Tidal height and frequency dependence of acoustic velocity and attenuation in shallow gassy marine sediments

Angus I. Best

Challenger Division for Seafloor Processes, Southampton Oceanography Centre, University of Southampton Waterfront Campus, Southampton, UK

Michael D. J. Tuffin

Challenger Division for Seafloor Processes, Southampton Oceanography Centre, University of Southampton, Southampton, UK

School of Ocean and Earth Science, Southampton Oceanography Centre, University of Southampton, Southampton, UK

Justin K. Dix and Jonathan M. Bull

School of Ocean and Earth Science, Southampton Oceanography Centre, University of Southampton, Southampton, UK

Received 20 August 2003; revised 17 May 2004; accepted 8 June 2004; published 5 August 2004.

[1] Remote prediction of gassy marine sediment properties is important for geohazard assessment. Gas bubble resonance theory suggests that gassy sediments exhibit acoustic wave velocity-frequency and attenuation-frequency relationships that depend on gas bubble size, gas content, and sediment elastic properties. An acoustic monitoring experiment to investigate gas bubble resonance effects was undertaken at an intertidal site at Dibden Bay, Southampton, United Kingdom. A vertical hydrophone array was positioned to straddle the top of the gassy zone identified on acoustic reflection profiles at about 1 m below the seabed. A miniboomer in the seabed above the array was used to generate broadband (600 Hz to 3000 Hz) acoustic signals every 10 min during a 24 hour period with water depths varying between 0 m (subaerial exposure) at low tide and 2.35 m at high tide. The calculated frequency spectra of compressional wave attenuation coefficient show an attenuation maximum (over 200 dB/m) that shifts in frequency from 1050 Hz at low tide to 1250 Hz at high tide, thus for the first time providing direct evidence of in situ gas bubble resonance in marine sediments. Modeling suggests that effective gas bubble radii of 11 mm to 13 mm are responsible for the attenuation maximum, supported by X-ray computed tomography scan observations on a pressure core (which also indicate that bubble shape depends on sediment type). Modeling of bubble size fluctuations due to pressure equilibration cannot reproduce the observed frequency shift of the attenuation maximum, implying that gas diffusion and nonspherical bubbles are significant. *INDEX TERMS:* 3022 Marine Geology and Geophysics: Marine sediments—processes and transport; 3025 Marine Geology and Geophysics: Marine seismics (0935); 3210 Mathematical Geophysics: Modeling; 4227 Oceanography: General: Diurnal, seasonal, and annual cycles; 4259 Oceanography: General: Ocean acoustics; *KEYWORDS:* acoustic, velocity, attenuation, gassy marine sediments

Citation: Best, A. I., M. D. J. Tuffin, J. K. Dix, and J. M. Bull (2004), Tidal height and frequency dependence of acoustic velocity and attenuation in shallow gassy marine sediments, *J. Geophys. Res.*, *109*, B08101, doi:10.1029/2003JB002748.

1. Introduction

[2] Free gas in marine sediments is often inferred from observations of high-amplitude returns and poor acoustic penetration on seismic reflection profiles [*Fleischer et al.*, 2001; *Schubel*, 1974]. Shallow (<20 m subseabed) gas is typically associated with the decomposition of organic matter by anaerobic bacteria and archaea [*Floodgate and Judd*, 1992]. The presence of gas and the physical properties of gassy sediments are of interest to a number of offshore activities, including drilling operations and the siting of seafloor structures [*Sills and Wheeler*, 1992]. Free gas, whether biogenic or petrogenic in origin, is also thought to influence the stability of sediments within the upper 500 m below the seabed in association with methane hydrates [*Mienert and Posewang*, 1999]. Although the causes of slope failures are poorly understood, it is known that gas bubbles lower the shear strength of marine sediments compared to their fully water saturated

0148-0227/04/2003JB002748$09.00

state [*Briggs and Richardson*, 1996; *Whelan et al.*, 1976]. Understanding the way in which free gas bubbles form in sediments, their effect on geotechnical properties, and their relationship with the hydrate stability zone [*Manley and Flood*, 1989] may give clues to the kind of environmental influences that generate slope instability [*Cochonat et al.*, 2002] and methane gas release from the seabed.

[3] The purpose of this study is to investigate the response of in situ gas bubbles to changes in hydrostatic pressure. This was achieved by monitoring the changes in acoustical properties of known shallow, gassy sediments over two complete tidal cycles. A forward model, based on the theory of the acoustical resonance behavior of gassy sediments developed by *Anderson and Hampton* [1980a, 1980b], was then used to make predictions about changes in gas bubble size. The validation of the theory was an equally important aim because, although there have been many observations of gassy sediments on seismic records, there have been no systematic, direct measurements of acoustic velocity and attenuation over a sufficiently wide bandwidth to demonstrate the predicted gas bubble resonance curves.

[4] There have been, however, several indirect observations that support the idea of gas bubble resonance in situ, notably work carried out in Eckernförde Bay near Kiel, Germany. *Tang* [1996] modeled the observed acoustic backscatter of shallow gassy sediments on the basis of the resonance of oblate spheroidal voids. *Fu et al.* [1996] found evidence that compressional wave velocity was both higher and lower in gassy sediments than in surrounding, nongassy sediments, as predicted by resonance theory. *Slowey et al.* [1996] observed low velocities in gassy sediment cores and high scattering on 30 kHz seismic profiles. *Lyons et al.* [1996] were able to replicate the observed signals from an acoustic reflection profile over a pockmark using *Anderson and Hampton*'s [1980a, 1980b] model with some corrections and modifications for nonspherical bubbles. *Wever et al.* [1998] observed annual changes in the depth of the top of the gassy zone and changes in backscatter strength, as observed on 3.5 kHz acoustic profiles.

[5] *Wilkens and Richardson* [1998] studied the frequency dependence of acoustic waves in shallow gassy sediments in Eckernförde Bay using a variety of measurement techniques, including 15 kHz and 30 kHz normal incidence reflection data, in situ probes (5–20 kHz, 38 kHz, 58 kHz, and also shear waves at 50–300 Hz), and laboratory pressure core data (400 kHz). They used the *Anderson and Hampton* [1980a, 1980b] model to interpret their results using a measured gas bubble size distribution. Although their excellent study provided convincing evidence for in situ gas bubble resonance effects that were consistent with the gas bubble size distributions observed on X-ray computed tomography (CT) scans of pressure cores, they were unable to measure continuous velocity-frequency and attenuation-frequency curves over a sufficiently wide bandwidth to unambiguously characterize the acoustical behavior of the gassy sediments. Their approach was also hampered by problems associated with colocating the various measurement techniques and possible heterogeneous gas distributions within the sediments.

[6] This paper presents the results of a single, in situ, acoustic monitoring experiment conducted over 24 hours (two complete tidal cycles) on shallow, subseabed, gassy sediments in an intertidal zone. These results provide, for the first time, direct evidence of gas bubble resonance in situ, consistent with theory, over the frequency range 600 Hz to 3000 Hz. Moreover, the estimated change in gas bubble size (assuming spherical bubbles) based solely on bubble pressure equilibrium changes in response to changes in hydrostatic pressure cannot account for the magnitude of the observed shift in resonance frequency. This suggests that other phenomena, such as gas diffusion and the presence of nonspherical bubbles, are important for controlling gas bubble shrinkage, expansion, and acoustical response in situ. X-ray CT results on a pressure core provide evidence for different bubble shapes according to sediment type.

2. Theory of the Acoustical Behavior of Gassy Sediments

[7] *Anderson and Hampton* [1980a, 1980b] developed a theoretical model to predict the effect of free gas on the velocity and attenuation of acoustic waves in marine sediments. In fact, the model is an extension of the theory of the acoustical behavior of gassy water by *Devin* [1959], *Eller* [1970], *Minnaert* [1933], and *Silberman* [1957]. The most interesting feature of the theory is that it predicts strong resonance effects resulting in frequency-dependent velocity and attenuation. At resonance the apparent cross-sectional area of a gas bubble becomes much larger than its actual physical size, and this leads to strong acoustic scattering and high signal attenuation. The scattering attenuation caused by gas bubble resonance is in addition to the intrinsic attenuation of the host sediment. By comparison, water-saturated marine sediments show relatively small, smooth changes in velocity and attenuation (Q^{-1}) over a wide range of measurement frequency [e.g., *Best et al.*, 2001; *Buckingham*, 1998; *Hamilton*, 1980; *Kibblewhite*, 1989; *Stoll*, 1985, 2002]. The resonance frequency of a gas bubble depends on the bubble radius; the thermal properties of the gas; the dynamic bulk and shear moduli of the sediment; the sediment bulk density; and the ambient hydrostatic pressure. The following expressions from *Anderson and Hampton* [1980b] can be used to derive the frequency-dependent phase velocity V and attenuation coefficient α (see Appendix A for full expressions):

$$\left(\frac{V_0}{V}\right)^2 = \frac{1 + a_s X_*}{2}\left\{1 \pm \left[1 + \left(\frac{a_s Y_*}{1 + a_s X_*}\right)^2\right]^{1/2}\right\} \quad (1)$$

and

$$\alpha = \frac{\pi f}{V_0}.\frac{V}{V_0}.\, a_s Y_*, \quad (2)$$

where

$$a_s = \frac{K}{\gamma P_0 + \frac{4}{3}G}, \quad (3)$$

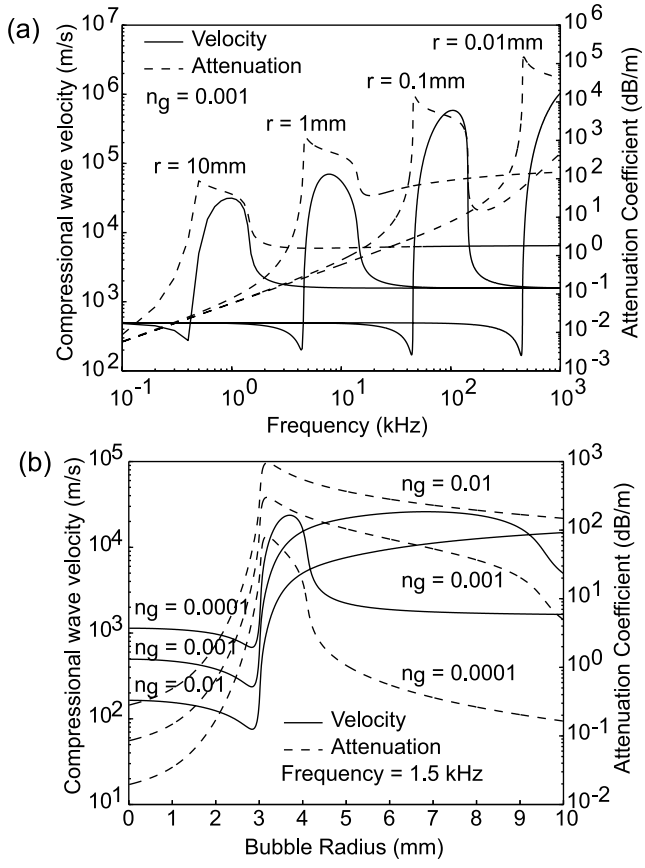

Figure 1. Acoustical response of gassy sediments according to the model of *Anderson and Hampton* [1980a, 1980b]. See Table 1 for model input parameters. Variation in acoustic velocity and attenuation coefficient with (a) frequency for a range of gas bubble sizes (constant gas content $n_g = 0.001$) and (b) bubble radius for a range of gas contents (constant frequency of 1.5 kHz).

V_0 is the acoustic velocity of the nongassy (fully water saturated) sediment, f is acoustic frequency, K and G are the nongassy sediment bulk and shear moduli, respectively, γ is the ratio of specific heats of methane gas, and P_0 is the ambient hydrostatic pressure. The parameters X_* and Y_* are frequency dependent and include terms for resonant frequency, gas fraction, and acoustic damping for a single gas bubble size. The resonant frequency f_0 is given by

$$f_0 = \frac{1}{2\pi r}\left(\frac{3\gamma P_0}{A\rho} + \frac{4G}{\rho}\right)^{1/2}, \tag{4}$$

where r is bubble radius, A is the gas polytropic coefficient, and ρ is sediment density. In particular, note that equation (4) relates the resonant frequency f_0 to the hydrostatic pressure P_0 and the gas bubble radius r.

[8] A typical set of response curves (Figure 1) shows three distinct zones of frequency-dependent behavior. The values of input parameters were measured from samples recovered from the Dibden Bay site (see sections 3 and 5) or taken from the literature (see section 6 and Table 1). If the insonifying frequency is lower than the resonance frequency of the gas bubble, then the velocity of the gassy sediment V is less than that of the nongassy sediment V_0. A transition zone is seen at frequencies near resonance where V dramatically increases, before gradually approaching the value of V_0 at frequencies above resonance. The model predicts velocities that seem unrealistically high at resonance, and these have yet to be seen in field data. The gas bubbles also cause a dramatic increase in attenuation coefficient at frequencies near resonance, the result of the large increase in apparent scattering cross-section area of the bubbles. Note that the attenuation coefficient calculated here is solely due to acoustical bubble scattering (which also includes terms for fluid viscous damping at the bubble walls, bubble radiation damping, and bubble gas thermal damping) and does not include contributions from the background, intrinsic attenuation (absorption) of the nongassy sediment. Attenuation due to scattering is generally considered to be insignificant in water-saturated marine sediments when wavelengths are much greater than the sediment grain size. Real gassy sediments will have a variety of bubble sizes that could lead to bubble resonance effects being detected across a range of frequencies.

[9] The experimental observations outlined below give direct evidence for acoustic gas bubble resonance in situ. Using reasonable input parameters, the above model predicts gas bubble sizes (on the basis of the observed resonance frequencies) that are similar to gas bubble sizes observed in pressure-sealed cores from the site. The observed variations in resonance frequency with tidal height (hence hydrostatic pressure P_0 and bubble radius r) are generally consistent with the model predictions, although the input parameters were not sufficiently well resolved to make accurate predictions of magnitude changes.

3. Dibden Bay Experimental Site

[10] Dibden Bay is an intertidal mud flat on the western shore of the upper reaches of Southampton Water, United Kingdom (Figure 2). It was chosen for a series of in situ acoustic experiments and geological sampling because there was ample evidence for shallow gas there. Also, its subaerial exposure at low tide gave some practical advantages

Table 1. Model Input Parameters

Parameter	Value
Water depth	0–2.35 m
Sediment depth	1 m
ρ_w	1030 kg m^{-3} [a]
V_0	1535 m s^{-1}
ρ	1612 kg m^{-3}
n	0.627
K	3.89 GPa
G	2.52 MPa
G'	123 kPa
ρ_g	0.717 kg m^{-3} [a]
s_p	2.19 J kg^{-1} °C^{-1} [a]
C_g	3.11 × 10^{-2} J s^{-1} m^{-1} °C^{-1} [a]
γ	1.31[a]
f	600–3000 Hz

[a]Values taken from standard tables of *Kaye and Laby* [1995].

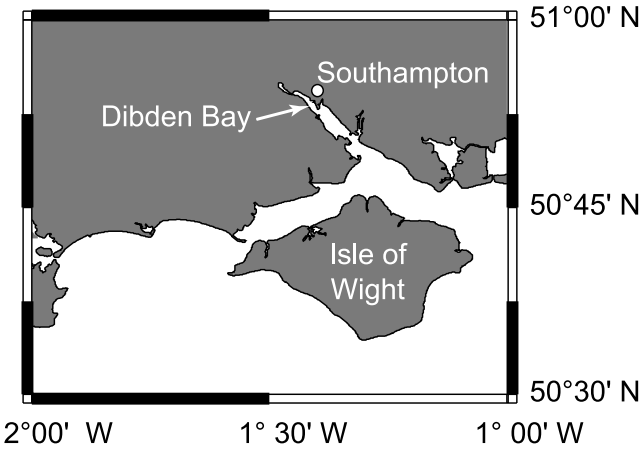

Figure 2. Location of Dibden Bay experimental site near Southampton, United Kingdom (UK National Grid Reference 442115, 108975).

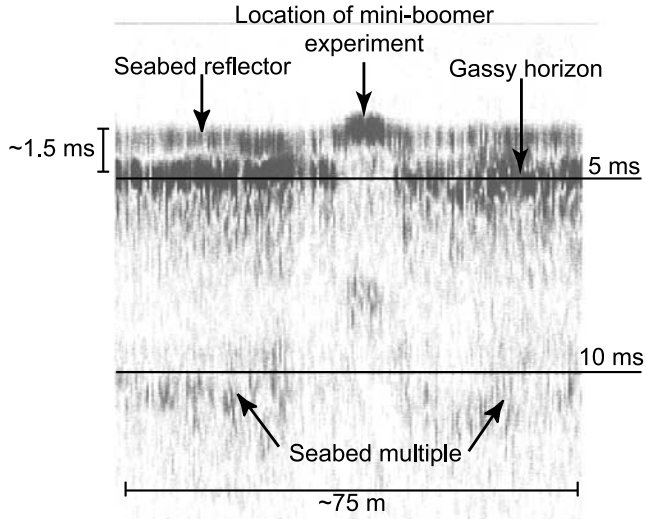

Figure 3. Normal incidence acoustic (chirp) reflection profile (frequency content 2–8 kHz) over the Dibden Bay experimental site showing high-amplitude reflections from the gassy horizon.

over wholly underwater sites. The sediments comprise very soft mud with a thin, surficial shell layer in some areas. The presence of free gas was inferred from acoustic turbidity observed on normal incidence acoustic chirp reflection profiles (frequency sweep 2–8 kHz; Figure 3) and the distinct odor of hydrogen sulfide in the mud, a good indicator of the anoxic conditions required by methanogenic archaea. The precise location of the experimental site (UK National Grid Reference 442115, 108975) corresponds to the domed area of high-amplitude reflections associated with a local surficial shell layer in Figure 3. A laterally continuous curtain of strong acoustic returns (starting at about 1.5 ms two-way travel time below the seafloor reflector) can be seen on either side of the domed area. Although this acoustic turbidity is not observed directly beneath the site, it is assumed that in fact gassy sediments are present, although masked by the strong reflections from the surface shell layer. An auger core taken at the site at low tide (see Figure 4) shows the sediments to be predominantly dark gray silt-clay with occasional thin sand stringers and abundant organic matter (ideal conditions for the generation of methane gas).

4. In Situ Acoustic Monitoring Experiment

4.1. Experimental Method

[11] A vertical hydrophone array and a miniboomer acoustic source were used to monitor the acoustic velocity and attenuation of the Dibden Bay sediments over two complete tidal cycles (24 hours) during March 2000. The source-receiver geometry was similar in concept to larger-scale vertical seismic profiling techniques [e.g., *Pujol et al.*, 1998]. The miniboomer uses a high-voltage inverter to drive a magnetopropulsive plate 20 cm in diameter. It produces a repeatable signal with a spherical radiation pattern and a spectral content between 0 and 11 kHz in water; the hydrophones have a flat frequency response from about 100 Hz up to 10 kHz [see *Best et al.*, 2001]. The hydrophone depths were chosen to ensure that at least one hydrophone was above the gas horizon and at least one was below it, as predicted using information from the chirp profile and auger core (see Figure 3 and Figure 4). Transmission data were recorded at 10 min intervals over 24 hours using a digital storage oscilloscope. Tidal height was calculated from tide gauge data collected routinely at the port of Southampton.

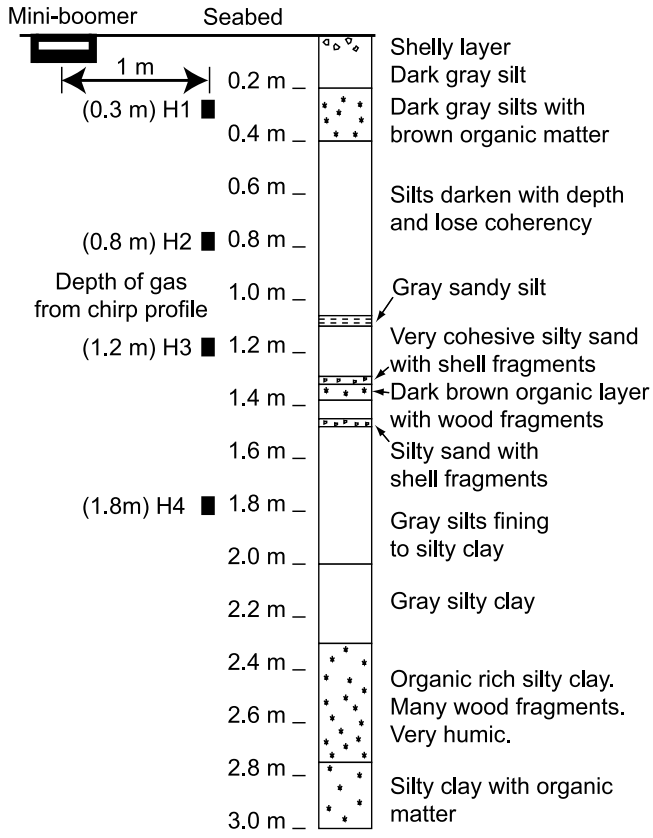

Figure 4. Experimental arrangement of the miniboomer and four hydrophone receivers (labeled H1 to H4). Sediment descriptions from an auger core at the site are also given.

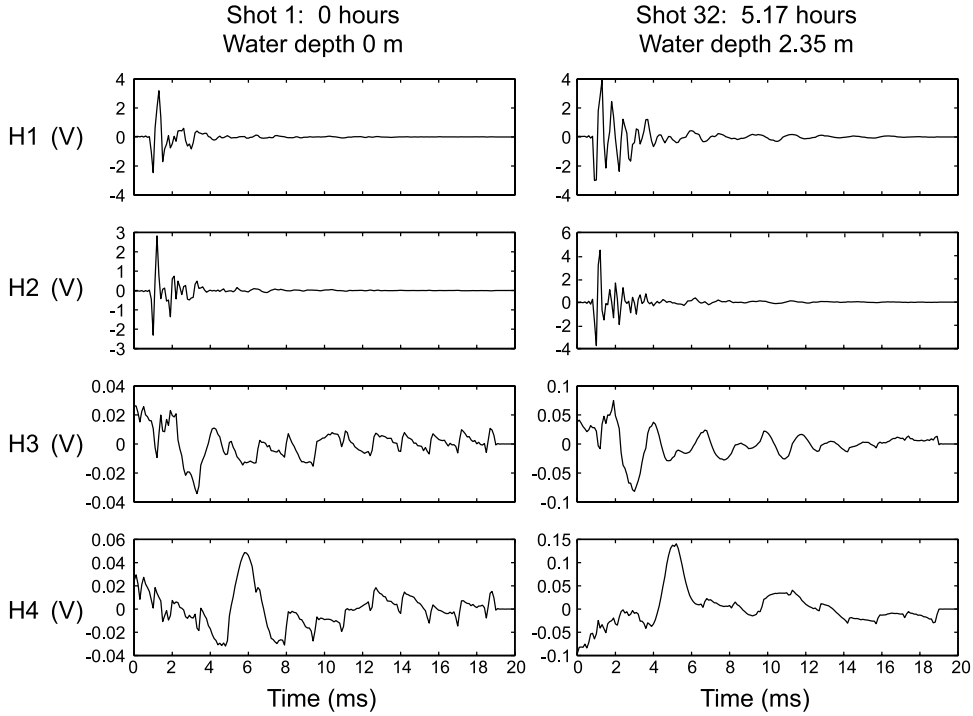

Figure 5. Example time series recorded at the four hydrophones H1 to H4 (see Figure 4) at low and high tide during the acoustic monitoring experiment.

4.2. Data Processing

[12] The time series data recorded for each shot were processed using the filter correlation method that is described fully by *Best et al.* [2001] and by *Courtney and Mayer* [1993]. The original time series were band-pass filtered into a sequence of 100 Hz frequency bands, from a minimum central frequency of 600 Hz to a maximum central frequency of 3 kHz. Frequencies less than 600 Hz and higher than 3 kHz were discarded as the signal-to-noise ratio was too low (approximately -60 dB relative to the maximum signal level). Pairs of time series were used to determine phase velocity and attenuation coefficient knowing the source-receiver geometry and source radiation pattern. A cross correlation was performed between each pair of filtered time series, for example, using the time series recorded at Hydrophone 1 (H1) and at Hydrophone 2 (H2), respectively. The time delay, corresponding to the global maximum of the cross-correlation function, was used to calculate the phase velocity V for each frequency band according to

$$V(f) = \frac{x_2 - x_1}{(T_2 - T_1) + \delta t(f)}, \tag{5}$$

where x_1 and x_2 are the source-receiver distances for (e.g.) H1 and H2, T_1 and T_2 are the start times of the windowed time series recorded at (e.g.) H1 and H2, δt is the cross-correlation delay time, and f is frequency. A single attenuation coefficient α (in dB/m) was determined for each frequency band, assuming a spherical spreading law, according to

$$\alpha(f) = 8.686 \frac{1}{\delta x} \ln \left| \frac{A_1(f)}{A_2(f)} \frac{x_1}{x_2} \right|, \tag{6}$$

where δx is the difference in source-receiver distances, and A_1 and A_2 are the root-mean-square energies for each windowed, band-pass-filtered signal recorded at (e.g.) H1 and H2. The computed velocity and attenuation coefficient values were assigned to the central frequency of each 100 Hz passband, corresponding to frequency f in equations (5) and (6).

[13] The main source of error in the velocity and attenuation calculations is the measured distance between receiver pairs, while time and amplitude measurement errors are negligible. The timing error was taken as double the sample interval of 1×10^{-7} s, the amplitude error was taken as double the amplitude precision of 1×10^{-6} V, and the source-receiver depth error was taken as ±2 cm. Simple summation of percentage errors for the H2-H3 calculations using equations (5) and (6) leads to a velocity accuracy of ±4.2% and an attenuation coefficient accuracy of ±8.3%, assuming perfect transducer coupling to the sediment. In a previous experiment [*Best et al.*, 2001] the miniboomer coupling was demonstrated to be repeatable both between shots and after replacement on the seabed; we did not check the quality and repeatability of the hydrophone coupling to the sediment. However, it is reasonable to assume that water will fill any cavities between the hydrophones and the adjacent sediment or that the soft sediment itself will close around the hydrophones, thus giving good coupling.

4.3. Example Time Series

[14] Example time series (common shot gathers) recorded at low and high tide are shown in Figure 5. There is a noticeable change in signal character both with tidal height and with hydrophone depth. The direct arrivals are clearly identifiable on H1 and H2, but it is difficult to discern coherent signals above the background noise on H3 and H4.

The dramatic fall in signal amplitude between H2 and H3 in both gathers indicates highly attenuating sediments; by contrast, there is little difference in signal amplitude between H1 and H2. The depths of H2 (0.8 m) and H3 (1.2 m) straddle the top of the gassy zone determined from the chirp data in Figure 3. The two-way travel time of the top of the gas horizon from the seabed is ~1.5 ms; using a compressional wave velocity of 1400 m s^{-1} measured at the site by *Tuffin et al.* [2000] gives a depth of 1.05 m.

[15] The spikes occurring at ~2 ms intervals on H3 and H4 are possibly caused by electrical interference from the oscilloscope power supply. However, a slight improvement in signal-to-noise ratio is evident with increasing tidal height for H3 and H4. This may be because electrical noise from the power supply is more attenuated by the overlying water at high tide. The data from H4 were the most severely affected by noise (possibly an amplifier electronics problem), having a severe baseline shift that decreased approximately exponentially with time after the trigger. The data in Figure 5 (H4) have been corrected for this baseline shift, although ultimately not to our satisfaction. Consequently, these data were excluded from the rest of the analysis.

4.4. Multiple Reflections

[16] Reverberations from strong reflectors such as the sea surface, the seabed, sand stringers, or even the top of the gassy zone could affect the velocity and attenuation results. In section 4.2 the whole time series recorded at each hydrophone was used as it was impossible to distinguish between direct arrivals and interfering multiples. Figure 5 shows clear evidence of reverberations after the first arrival, certainly for H1 and H2; they probably occur also for H3 and H4, although all arrivals are difficult to distinguish by eye above the background noise on these records. A simple analysis shows that interference fringes (maxima and minima) might be expected when the multiple path length exceeds the direct path length between the source and the receiver by a factor of $\lambda/2$ (where λ is the wavelength). This distance can be related to frequency f_i by the expression $f_i = c/2\delta l$, where c is the average velocity (water or sediment) and δl is the difference in path length. For the sea surface multiple, δl is approximately twice the water depth, and f_i is expected to give a $1/4\delta l$ dependence ("U"-shaped curve) on the frequency-depth (or time) chart in Figure 6, with the "U" minimum at high tide and the "U" limbs going to infinity at low tide (zero water depth). By contrast, multiples from within the sediment column are expected to give interference patterns at frequencies that do not vary with water depth (or time) because δl will remain constant.

[17] In fact, the velocity and attenuation results (see below) show interference fringes that are consistent with the above predictions for both sea surface and sediment column multiples. Neither their time variance nor frequency magnitude seem to affect the main observations of gas bubble resonance discussed below.

4.5. Velocity and Attenuation Results

[18] The compressional wave phase velocity and attenuation coefficient results are shown in Figures 6a and 6b, respectively, as a function of frequency (ordinate) and time (abscissa); the water depths corresponding to the shot times are indicated. Results for all three useable receiver pairs are presented (H1 and H2; H1 and H3; H2 and H3).

[19] In general, phase velocity and attenuation show complex dependencies on water depth and frequency, although at least some of these phenomena can be explained by interference effects from reverberations (see above). In particular, the "U"-shaped curves seen for all receiver combinations, for both velocity and attenuation, are consistent with interference from the water column multiple on H1 and H2 records. Interference fringe frequencies show minima at both high tides and go to infinity as water depth goes to zero, as predicted in section 4.4. The most likely candidate for the high velocity and attenuation bands at about 1800 Hz (no change with time or water depth) for H1-H2 and H1-H3 results (very faintly seen on H2-H3 results) are seabed multiples on H1 and H2 records corresponding to the miniboomer burial depth of 0.22 ± 0.02 m. Most importantly, these multiple effects do not obscure the main observation attributed to gas bubble resonance discussed below. This is because the seabed multiple occurs at much higher frequencies than the resonance peak at 1050–1250 Hz, and the data processing method detects the stronger resonance effect in preference to the weaker sea surface multiple effect at those frequencies where the two phenomena coincide.

[20] The hydrophone pair H1-H2 should give, in the absence of free gas, some indication of the water-saturated sediment properties, assuming there is no significant lithological variation over the depth interval. In fact, H1-H2 velocity is generally under about 1000 m s^{-1} (blue colors), except for the high-velocity band at about 1700 Hz to 2000 Hz (probably a multiple effect; see above) that extends over both tidal cycles. The expected velocity for silt-clay is about 1550 m s^{-1} [*Hamilton and Bachman*, 1982], although a previous study at the site [*Tuffin et al.*, 2000] indicated a value of 1400 m s^{-1}, but this is still not as low as the observed background values; the reason for this is unclear. Most significantly for this study, the H1-H3 and H2-H3 results (but not the H1-H2 results) show distinct zones of zero velocity (dark blue) at about 1100 Hz that mimic the strong frequency dependence observed on the attenuation results discussed below. Zero velocity is taken to indicate signal-to-noise ratios too low to resolve phase information (i.e., in the presence of very high signal attenuation).

[21] The attenuation coefficient results offer the most telling insight into the acoustical behavior of gassy sediments in situ. By comparison with the H1-H3 and H2-H3 results, the H1-H2 results show relatively low attenuation coefficients (generally below 50 dB/m). By contrast, the attenuation coefficients seen on the H1-H3 results are generally above 100 dB m^{-1} and above 150 dB m^{-1} for the H2-H3 results. The most significant features for H1-H3 and H2-H3 are the strong frequency-time (water depth) dependent, narrow bands of high attenuation (in excess of 200 dB m^{-1} for H2-H3) at about 1100 Hz. These observations are consistent with the notion of increasing resonance frequency of gassy sediments with decreasing bubble size, as would be expected for increasing water depth and hence increasing hydrostatic pressure. Note that the attenuations for H1-H3 are lower than for those for H2-H3. We postulate that nearly all the signal attenuation is occurring between H2 and H3, and the normalization to unit distance traveled

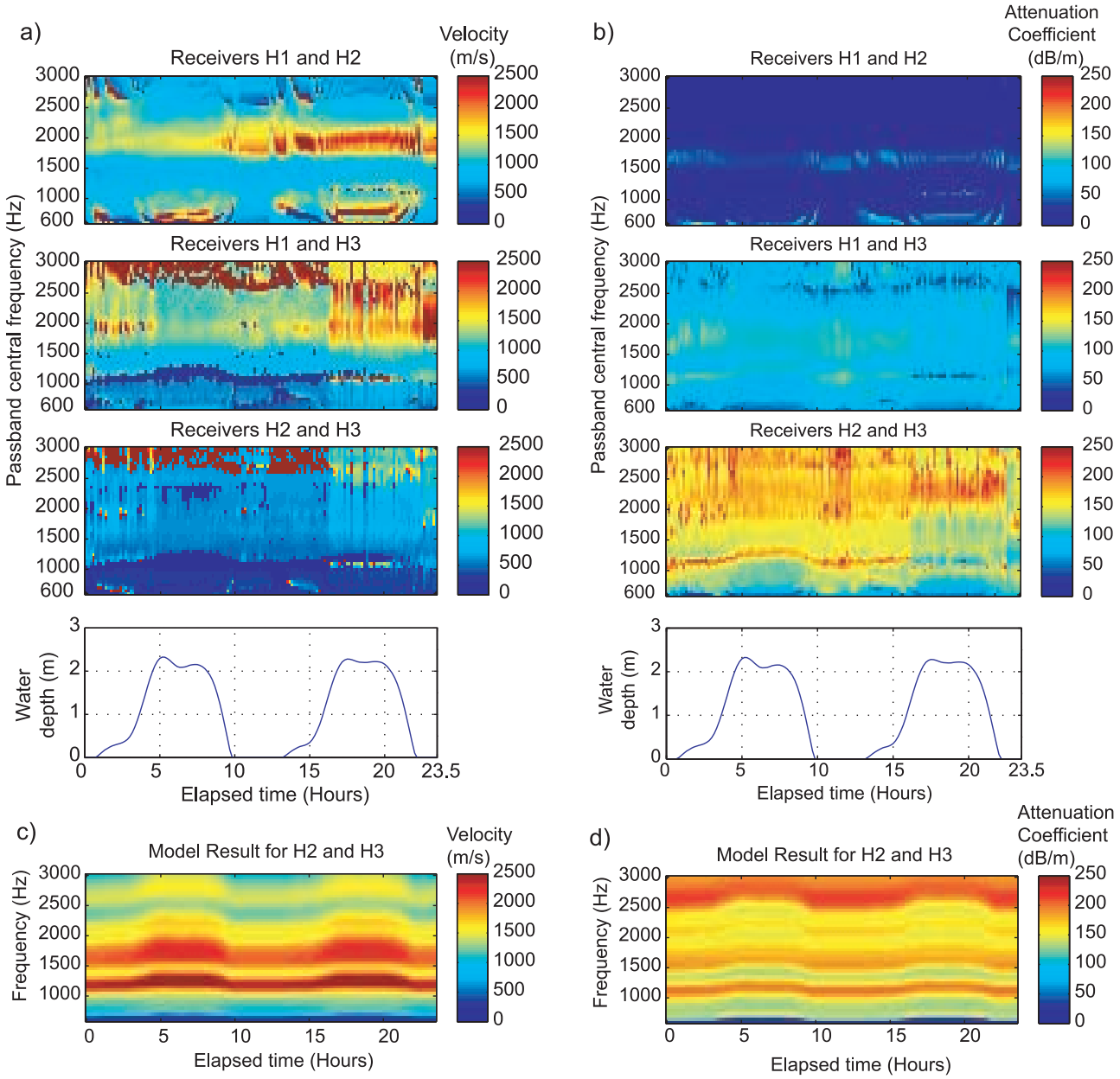

Figure 6. Acoustic monitoring results: (a) velocity and (b) attenuation coefficient versus frequency (600–3000 Hz) over a complete tidal cycle. Hydrophone pairs used in the processing (see text) are indicated, as is water depth. Model results are shown for (c) velocity and (d) attenuation coefficient.

by the acoustic wave leads to a lower dB m^{-1} value for H1-H3.

[22] There seems to be an abrupt change in the character of the recorded spectra over the last quarter-tidal cycle in, for example, Figure 6b (H2-H3). This is possibly due to electrical interference or instrument problems (e.g., ingress of water into cables); the results prior to this seem to be of consistent quality.

5. Laboratory Analysis of Sediment Cores

5.1. Core Analyses

[23] The aim of the laboratory analysis program was to provide as many input parameters as possible for the gassy sediment acoustic model (see Table 1 for a list of the required parameters). In October 2000, two 15 cm square-section Kastenlot cores (lengths 3 m and 2 m) and two 3 m long pressure cores (internal diameter 10.8 cm) were collected at the site, deployed from a barge at high tide (see, e.g., *Weaver and Schultheiss* [1990] for more details on gravity coring techniques). The pressure cores used novel, gas-sealing end caps that were inserted in each end of the plastic core barrel by divers before the cores were brought to the surface [*Tuffin*, 2001]; the aim was to maintain the in situ hydrostatic pressure within the cores as far as possible. The Kastenlot cores were used for destructive tests, while the pressure cores were collected primarily to image gas bubbles and to obtain information on their size and distribution.

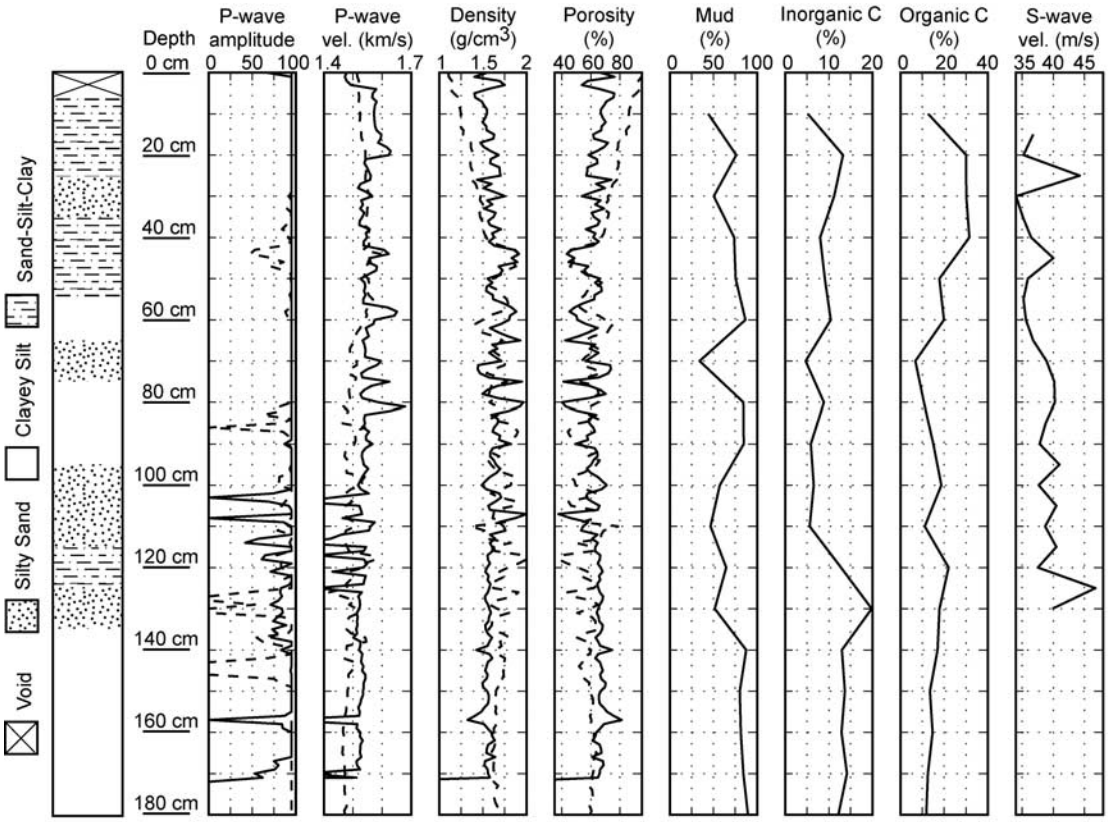

Figure 7. Core analysis results obtained on the Kastenlot core KDIB1 (solid line) and the pressure core PDIB1 (dashed line); see text. Sediment classification of KDIB1 from grain size analysis according to *Shepard* [1954] is also shown. *P* wave vel., compressional wave velocity; *S* wave vel., shear wave velocity; Organic C, organic carbon content; Inorganic C, inorganic carbon content; Mud, silt and clay fraction.

[24] Compressional wave (*P* wave) velocity and amplitude (at a frequency of about 500 kHz) and bulk density were measured at 1 cm intervals on the cores using a multisensor core logger [*Best and Gunn*, 1999; *Gunn and Best*, 1998; *Schultheiss and Weaver*, 1992]. Porosity was calculated from the density readings assuming constant seawater and mineral bulk densities (1024 kg m^{-3} and 2650 kg m^{-3}, respectively [see, e.g., *Boyce*, 1976]). Shear wave velocity was measured at 10 cm intervals on the fresh Kastenlot cores using bender elements [see, e.g., *Shirley and Hampton*, 1978] inserted into the exposed sediment before subsampling, also at 10 cm intervals. Organic and inorganic carbon content and grain size analysis were performed on the subsamples using standard methods [*Engleman et al.*, 1985; *McManus*, 1991; *Stein*, 1985]. Undrained shear strength was measured on the Kastenlot cores using a handheld vane tester [see *British Standards Institution*, 1990]. More details of the core analyses are given by *Tuffin* [2001].

[25] The sedimentary log in Figure 7 shows predominantly muddy sediments with sandy layers centered at about 30 cm, 70 cm, 110 cm, and 130 cm depth; the log was constructed from visual inspection of the Kastenlot cores, subsample grain size analysis, and classification according to *Shepard* [1954]. Comparison of the multisensor logs of one Kastenlot core (KDIB1) and one pressure core (PDIB1) shows some interesting differences. Note that because of sediment slumping at the top of the pressure core (the Kastenlot core has low disturbance and good depth preservation), the pressure core log depths were adjusted to match the Kastenlot core log depths using the distinctive double peak in density at about 45 cm. All logs show fine-scale fluctuations even within zones of the same sediment classification. For example, relatively high *P* wave velocities (and correspondingly high densities) at 60 cm, 70 cm, 75 cm, and 80 cm depth are probably associated with sand stringers in the mud, although these are not resolved in the sedimentary log. There is some evidence for a fall in *P* wave velocity relative to overlying sediments (and more dropouts in *P* wave amplitude) below about 100 cm (Kastenlot core) and 60 cm (pressure core), respectively. The pressure core velocities are significantly lower than the Kastenlot core velocities below about 60 cm (velocity relative accuracy is ±1%). This is possibly due to gas bubble resonance effects, implying that there are sufficient small bubbles (<0.1 mm radius; see Figure 1) present in the pressure core (with resonance frequencies above the measurement frequency of 500 kHz) to cause a drop in velocity but not in the Kastenlot core. The fact that these

lower velocities in the pressure core appear above the top of the expected gassy zone (i.e., at 1 m depth) could indicate vertical migration of gassy water up the sides of the core barrel. These small bubbles will have a negligible effect on density. By contrast, zones of intense amplitude dropouts occur both on the Kastenlot core (100 cm to 140 cm) and on the pressure core (80 cm to 150 cm). If P wave amplitude dropouts are indicative of large gas cavities, then this suggests some preservation of these cavities in the Kastenlot core (due to either in situ methane gas or air that has ingressed into the exposed cavities, or both) even though some may have collapsed. In general, the depths of amplitude dropouts are similar in each core.

[26] Between about 40 cm and 100 cm depth, density and porosity show similar values for both the Kastenlot and the pressure core (above 40 cm, the pressure core density is lower, and porosity is higher, probably because of sediment slumping). Below about 100 cm the pressure core density shows larger fluctuations, and appears higher, than the Kastenlot core density (corresponding trends are seen in porosity, which appears lower in the pressure core). The fluctuations could be explained by the presence of large intact gas cavities that are not so well preserved in the Kastenlot core. The reason for the apparent low density and high porosity in the pressure core is unclear (perhaps a logger calibration issue). Log porosities of around 60% are typical for muddy sediments (mud contents generally greater than 50%), while organic carbon content is quite high (generally >10%) and inorganic carbon content is quite low (generally <10%, except at 130 cm, where there is a shell layer, also seen in the auger core log in Figure 4).

[27] Shear wave velocity ranges from about 35 m s^{-1} to 45 m s^{-1} and generally increases with depth. There is some evidence for more rapid depth fluctuations within the gassy zone below about 90 cm depth. Undrained shear strength tests gave an average value of 6 kPa (standard deviation ±2 kPa).

5.2. Elastic Moduli

[28] The bulk modulus of the water-saturated sediment K was calculated in two ways. The first method, which is thought to give the best values for elastic moduli [*Hamilton*, 1971], uses the result from the one-dimensional (1-D) wave equation for the compressional wave velocity V_p,

$$V_p = \left(\frac{K + \frac{4}{3}G}{\rho}\right)^{1/2}, \tag{7}$$

where G and ρ are the nongassy sediment shear modulus and density, respectively. The dynamic shear modulus G was calculated from measurements of shear wave velocity V_s according to

$$V_s = \left(\frac{G}{\rho}\right)^{1/2}. \tag{8}$$

The elastic moduli K and G were calculated for one Kastenlot core (KDIB1) and one pressure core (PDIB1). Since no measurements of shear wave velocity could be made on the pressure core, the dynamic shear modulus was calculated using the density measurements for the pressure core and the shear wave velocity measurements from the Kastenlot core. The compressional wave velocity measurements were then used to calculate the bulk modulus of the sediment.

[29] The second method involved the calculation of the bulk modulus according to *Gassmann* [1951] with the bulk modulus of the frame K_f calculated using the regression equation of *Hamilton* [1971] for silty clays:

$$K = K_s \frac{K_f + Q_g}{K_s + Q_g}, \tag{9}$$

$$Q_g = \frac{K_w(K_s - K_f)}{n(K_s - K_w)}, \tag{10}$$

$$\log(K_f) = 3.73580 - 4.25075n. \tag{11}$$

The parameters K_s and K_w are the bulk moduli of the mineral grains and pore water, respectively; n is fractional porosity. Note that in equation (11), K_f is in dyne $cm^{-2} \times 10^8$ (1 Pa = 10 dyne cm^{-2}). A value of 54.4 GPa was assumed for the bulk modulus of the mineral grains (clayey silt, San Diego Trough [*Hamilton*, 1971]) on the basis of the value of K_f at zero porosity in equation (11). The bulk modulus of the pore water was calculated using equation (7) with $G = 0$, a compressional wave velocity of 1489.8 m s^{-1} (the value for seawater at 10°C and salinity 35‰), and a density of 1030 kg m^{-3} [*Kaye and Laby*, 1995].

[30] Both the first and second methods of computing the in situ bulk modulus of the host sediment suffer from uncertainties associated with the unknown frequency dependence of velocity between ultrasonic core measurements and the in situ acoustic experiments, as well as from the DC assumptions of the Gassmann model. However, any velocity dispersion in the host (water-saturated) sediment is assumed to be negligible compared to that caused by gas bubble resonance effects.

[31] The results are presented in Table 2 as mean values, range of values, and standard deviations. Values of P wave velocity, bulk modulus, shear modulus, density, and porosity from the Kastenlot core were chosen to represent the water-saturated (nongassy) host sediment. The imaginary shear modulus of the sediment was estimated by assuming that the shear wave quality factor is equal to the compressional wave quality factor of 20.5, measured in a previous horizontal transmission experiment at the site [*Tuffin et al.*, 2000]. The imaginary shear modulus is equal to the shear modulus divided by the shear wave quality factor [*Toksöz and Johnston*, 1981]. The remaining model input values were taken from the literature (see Table 1).

5.3. X-Ray Computed Tomography Imaging

[32] X-ray computed tomography (CT) scans have been used successfully to image bubble size distributions in gassy sediments by, for example, *Anderson et al.* [1998], *Orsi et al.* [1994], and *Wilkens and Richardson* [1998]. X-ray CT scans were performed on one of the Dibden Bay pressure cores (PDIB1) to confirm the presence of gas bubbles in situ

Table 2. Physical Properties Measured on Cores[a]

Parameter	Pressure Core PDIB1	Kastenlot Core KDIB1
P wave velocity, m s^{-1}	1508 ± 4.9 (1418–1594)	1535 ± 8.3 (1243–1679)
S wave velocity, m s^{-1}	–	38.5 ± 1.3 (34.0–46.8)
Density, kg m^{-3}	1582 ± 25 (1105–2002)	1612 ± 17 (1325–2004)
Porosity, %	63.2 ± 1.8 (37.7–95.2)	62.7 ± 1.1 (37.6–81.1)
Bulk modulus,[b] GPa	3.75 ± 0.17 (2.97–4.46)	4.07 ± 0.21 (2.96–5.14)
Bulk modulus,[c] GPa	3.90 ± 0.28 (2.75–5.22)	3.89 ± 0.18 (3.45–5.01)
Shear modulus, MPa	2.42 ± 0.20 (1.69–3.55)	2.52 ± 0.18 (2.00–3.44)

[a]Average values with standard deviation, and range of values (in brackets) are given.
[b]First method (see text).
[c]Second method (see text).

and to estimate their size, shape, and number density. The example images in Figure 8, corresponding to core depths 132 cm (Figure 8a), 149 cm (Figure 8b), 151 cm (Figure 8c), and 175 cm (Figure 8d), show conclusive evidence of in situ gas bubbles at the site. The air surrounding each core image gives a suitable reference gray level for gas within the core. Sediment disturbance was considered minimal on the basis of our experience of using gravity corers in marine sediments. Unfortunately, the scans were obtained only in the depth range 1.2 m to 1.8 m (slightly below the depth range for the acoustical H2-H3 results of 0.8 m to 1.2 m). However, the auger core and Kastenlot core sedimentary logs indicate similar sediment types in both depth ranges. Combined with the *P* wave amplitude dropout evidence in Figure 7 (i.e., gassy sediments occur below ~1 m depth), it is reasonable to assume that the following scan observations apply also to the sediments in the depth interval of the acoustical results.

[33] The gas bubbles show different shapes according to the host sediment. While subcircular (presumably subspherical in three dimensions, diameter ~2 mm) bubbles form in silty sands (Figure 8a), sometimes coalescing to form larger, irregular bubbles up to ~10 mm diameter, most bubbles are observed in the clayey silts that predominate in the core (Figure 8b and Figure 8c). These "bubbles" in fact appear as low aspect ratio cavities, or cracks, up to ~40 mm long (intermediate axis), with their longest axes aligned in the subvertical plane (this was evident from the Kastenlot cores). Both the silty sand-hosted and mud-hosted bubbles are Type III bubbles according to the classification of *Anderson et al.* [1998] and *Wheeler* [1988]. Type I and Type II bubbles are well below the resolution of the X-ray scanner (~0.5 mm), although bubbles with radii as small as 0.1 mm have been observed by *Gardner and Goringe*

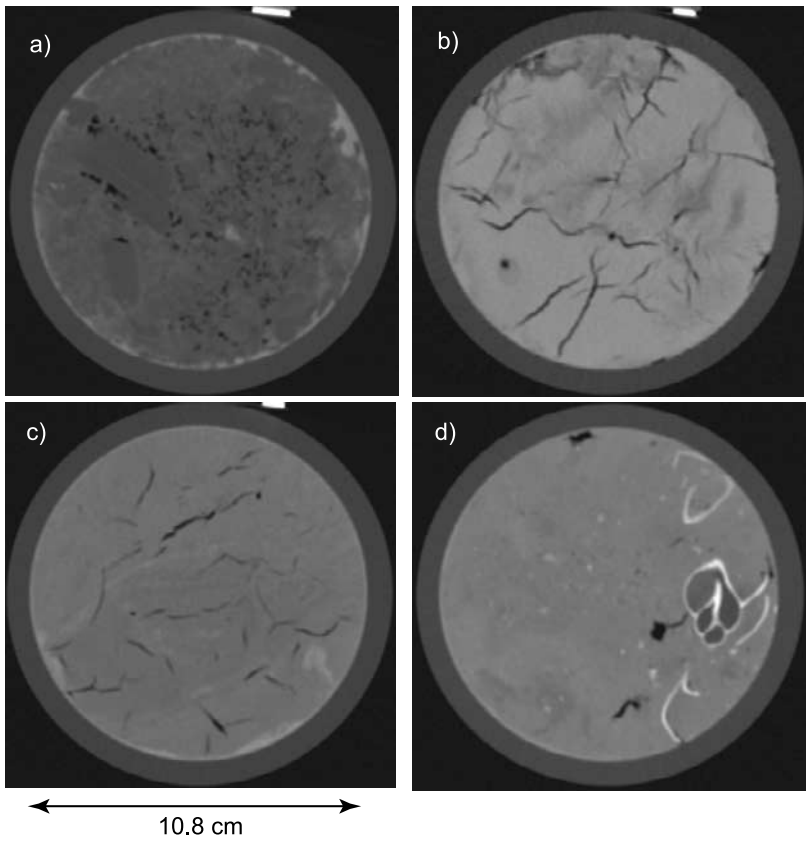

Figure 8. Example X-ray CT scan slices through the pressure core PDIB1. Core depths are (a) 132 cm, (b) 149 cm, (c) 151 cm, and (d) 175 cm. Black pixels indicate low density, e.g., air surrounding the core, or gas bubbles and cracks in Figures 8a–8c, while white pixels indicate high density, e.g., calcite shell in Figure 8d.

[1988]. The crack-like shape of the mud-hosted bubbles is at odds with the acoustical model that uses spherical cavities. One implication might be acoustical anisotropy, although our results are for acoustic propagation in the subvertical direction only. *Lyons et al.* [1996] developed an acoustical model for oblate spheroids in sediments based on the work of *Weston* [1967] and *Anderson and Hampton* [1980b]. Their results showed small increases in scattering attenuation and small decreases in resonance frequency for oblate compared to spherical bubbles.

[34] Other gas cavities are associated with intact calcium carbonate shells from gastropods, such as those in Figure 8d (the gray level inside the cavity may indicate partial water flooding in this case).

6. Modeling the Acoustical Behavior of Gassy Sediments in Dibden Bay

6.1. Effect of Changes in Hydrostatic Pressure

[35] The tidal range observed during the monitoring experiment at Dibden Bay was 0–2.35 m. This represents an increase in hydrostatic pressure from approximately 10 kPa to 34 kPa over a 6 hour period, assuming a depth of 1 m to the gas horizon and a water density of 1030 Kg m^{-3} [*Kaye and Laby*, 1995]. Hence the *Anderson and Hampton* [1980a, 1980b] model was adjusted to calculate variations in acoustic resonance characteristics with tidal height at the Dibden Bay site using measured input parameters as far as possible (see section 6.4). Two mechanisms for gas bubble shrinkage/expansion under changing hydrostatic pressure were considered: pressure equilibrium and diffusion.

6.2. Pressure Equilibrium

[36] Estimates of the pressure inside a gas bubble can be made by considering the conditions in the surrounding water-saturated sediment. Limits on the internal pressure of a gas bubble were proposed by *Wheeler et al.* [1990], who concluded that the internal pressure of a bubble was equal to the pore water pressure plus a surface tension term determined by the radius of curvature of the meniscus. Although *Wang et al.* [1998] provided a model for calculating the variation in pore pressure with depth in a sediment due to tides (i.e., the pore pressure requires a finite length of time to equilibrate with the changing hydrostatic pressure due to the generally low permeability of marine sediments), the shallow depth of the Dibden Bay gas permits the assumption that the pore pressure in the sediment is at all times equal to the hydrostatic pressure (also a common assumption in the field of soil mechanics [e.g., *Craig*, 1992]).

[37] Surface tension effects can be small compared to pore pressure effects, depending on the bubble radius. If it is assumed that the pore water pressure is approximately equal to the gas pressure, the radius of curvature of the meniscus is equal to the radius of the cavity. For a bubble radius of 0.1 mm and a surface tension coefficient of 0.073 N m^{-1} (the value for an air-water mixture), surface tension is 1460 N m^{-1}; for a bubble radius of 1 mm, the surface tension is 146 N m^{-1}. The X-ray CT images in section 5.3 suggest that bubble radii in Dibden Bay (and elsewhere [e.g., *Anderson et al.*, 1998; *Gardner and Goringe*, 1988]) are predominantly larger than 0.1 mm. Therefore surface tension effects were omitted from this analysis.

[38] If the bubble exists in equilibrium with its surroundings, there must be an increase in the internal pressure of the bubble to match any increase in the pore water pressure. In the absence of any mass transfer into the bubble, there is a decrease in bubble volume and hence a decrease in bubble radius. The change in bubble radius results in a change in the acoustical resonance frequency of the gassy sediment. Assuming the gas conforms to the Ideal Gas Law and there is no temperature change within the sediment during the adjustment, the final bubble radius may be calculated from

$$r_1^3 = \frac{P}{P_1} r_0^3, \tag{12}$$

where r_0 and r_1 are the initial and final gas bubble radii, respectively, and P and P_1 are the initial and final hydrostatic pressures, respectively. A decrease in hydrostatic pressure will result in an increase in bubble radius using the same argument.

[39] Each time the bubble radius changes, there will be an associated change in the gas porosity. For example, in a sediment containing 10 mm radius bubbles at a gas porosity of 0.001, for every 1 m^3 of sediment there are 0.001 m^3 of gas. Each bubble contains 4188.8 mm^3 of gas, so there must be 239 bubbles in that cube of sediment. If the bubble radius decreases by 1 mm, the total volume of gas becomes 0.00073 m^3, reducing the gas porosity to 0.00073, a change of 27%. Therefore the model was adapted to calculate a new gas porosity for each change in bubble radius according to the new total volume of all gas bubbles.

6.3. Gas Diffusion

[40] Although gas solubility is affected by changes in pressure according to Henry's law [*Abegg and Anderson*, 1997], diffusion is the mechanism by which gas migrates from the bubble to the pore water. Hence diffusion will determine any change in bubble size. The following expression for predicting the radius of a growing bubble, r, as a function of time t was proposed by *Boudreau et al.* [2001]:

$$r(t) = \left[\frac{nD}{2c_g}\left\{\frac{SR^2}{3D} + (c_1 - c_0)\right\}t + r_0^2\right]^{1/2}, \tag{13}$$

where r_0 is the initial bubble radius, R is the distance between bubbles, n is porosity, S is the local rate of methanogenesis, D is the diffusivity corrected for tortuosity, c_0 is the gas concentration in the pore water at bubble radius r, c_1 is the ambient gas concentration, and c_g is the gas concentration in the bubble. Consider a gas bubble at equilibrium with the surrounding water-saturated sediment. A small reduction in bubble volume, such as that caused by an increase in hydrostatic pressure, will lead to a small increase in c_g (small enough that $c_0 \leq c_1$); hence diffusion will act to slow down the rate of bubble growth. However, a large reduction in bubble volume (and associated increase in c_g) will lead to sediment undersaturation ($c_0 > c_1$) that may outweigh the local rate of gas production (methanogenesis); this will result in a net reduction in bubble volume and radius. If there is insufficient undersaturation, the bubble will continue to grow, albeit at a slower rate.

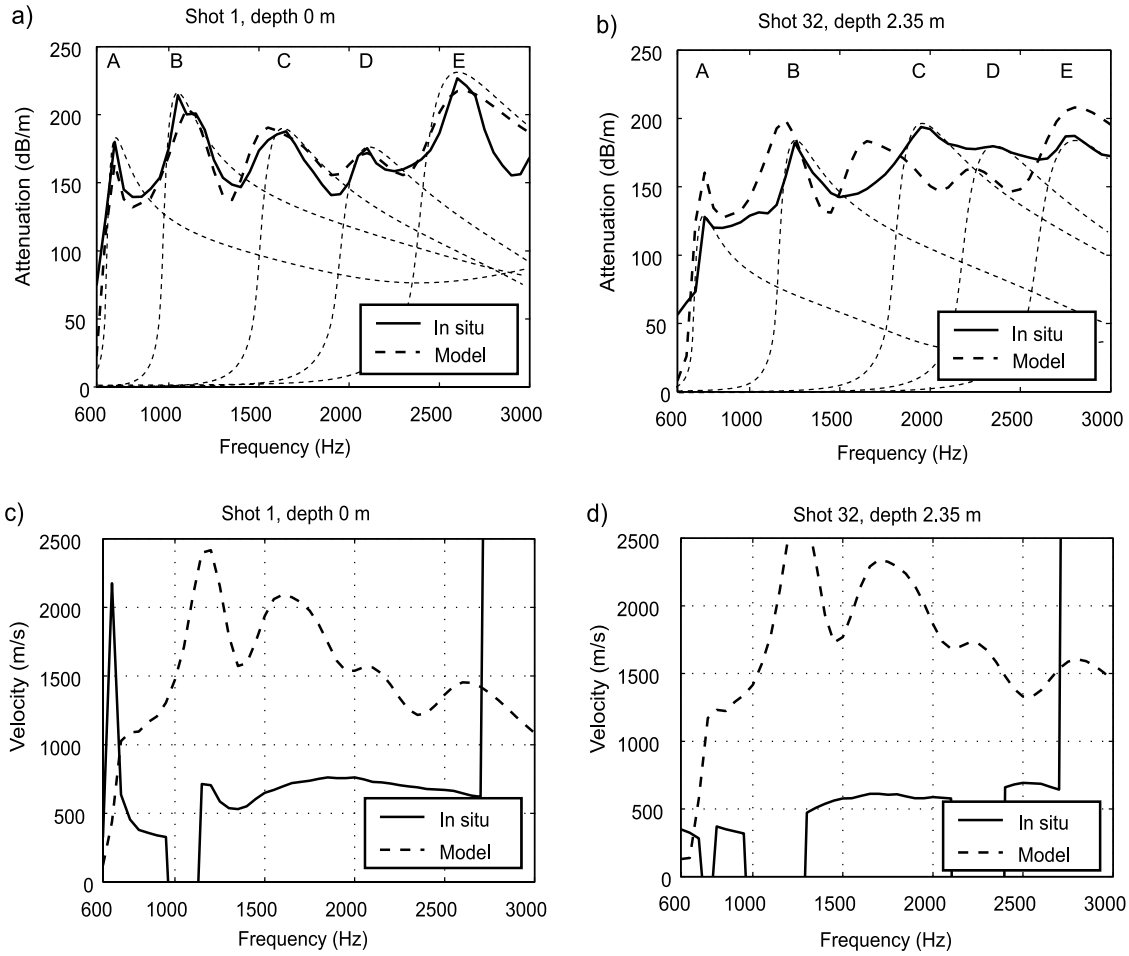

Figure 9. Example results for hydrophones H2-H3. Comparison of observed (solid line) attenuation coefficient (Figures 9a and 9b) and velocity (Figures 9c and 9d) spectra with model results at low (Figures 9a and 9c) and high (Figures 9b and 9d) tide. The model results are based on bubble resonance for single gas bubble sizes (thin dashed lines) and the overall response for the bubble size distribution in Figure 10 (thick dashed lines). The modeled attenuation maxima are labeled A to E, each assumed to correspond to resonance of a single gas bubble size.

[41] With sufficient chemical data it should be possible to use this model to calculate the effect of increasing c_g on the radius of a gas bubble, but in the absence of the required chemical data it was assumed that there is no net change in gas bubble radius due to diffusion, and the diffusion mechanism was omitted from the model. However, its importance may be estimated from the time it takes for the diffusive process to occur. The time t for a diffusive adjustment over a distance L is given by Einstein's relation,

$$t = \frac{L^2}{2D}, \tag{14}$$

where D is the diffusivity corrected for tortuosity. In the case of gas bubbles in sediment, L is of the order of the bubble radius, and D is of the order 10^{-5} cm^2 s^{-1} [*Boudreau et al.*, 2001]. Bubbles in the Dibden Bay pressure cores (see section 5.3) were between 1 mm and 10 mm in radius, corresponding to diffusion times between approximately 8 min and 14 hours, respectively. This indicates that some bubbles might undergo significant diffusion during the period of a tidal cycle, assuming saturation conditions are conducive.

6.4. Model Implementation and Bubble Size Distribution

[42] Although most of the model input parameters can be measured (see section 5), or estimated using values from the literature (see Table 1), the main unknowns are the initial bubble size distribution and associated gas porosities. It is relatively straightforward to fit the model output to a single attenuation resonance peak by adjusting the bubble radius and gas porosity. However, when there is a distribution of gas bubble sizes, which is more likely in the case of real marine sediments (borne out by the X-ray CT results in section 5.3), the modeled attenuation coefficient-frequency response curve for each resonance peak or bubble radius will affect the response curves of the other bubbles in a complex manner (determined by equations (A1) to (A17) in Appendix A) and will lead to a composite attenuation spectrum.

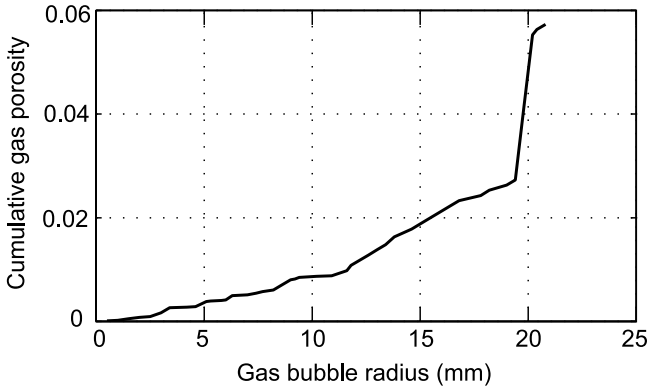

Figure 10. Gas bubble size distribution giving the best model fit to the observations at low tide in Figure 9a (water depth 0 m).

[43] Example attenuation coefficient-frequency and velocity-frequency response curves from the Dibden Bay 24 hour experiment are provided in Figure 9 (for hydrophones H2 and H3 only). The identified resonance peaks are labeled A–E in Figures 9a and 9b, and their details are given in Table 3. We used an arbitrary, linear function of cumulative gas porosity versus gas bubble radius (based on the single bubble size curve fitting exercise) that was adjusted to match the model output to the observed magnitudes of attenuation coefficient and resonance frequency. Shown in Figure 9a and Figure 9b are the fitted model curves for each resonance peak (thin dashed lines), assuming a single bubble size and gas porosity (see Table 3). Also shown are the composite model curves (thick dashed lines) fitted to the observations by further adjusting the bubble size distribution and gas porosity function to take into account the interactions between resonance peaks (a heuristic method was adopted). The best fit bubble size distribution and gas porosity function for shot 1, water depth 0 m, is given in Figure 10.

[44] The model was then run in the following way to predict the acoustical effects of changing gas bubble size and porosity due to changing water depth: (1) input initial environmental parameters and initial distribution of bubble radii and associated gas porosities; (2) check tidal height and calculate ambient hydrostatic pressure; (3) adjust each bubble radius and gas porosity for the next hydrostatic pressure increment (i.e., due to the change in water depth over a 10 min tidal period); (4) calculate parameters X_* and Y_* (see equations (A4) and (A5) for each bubble radius and associated gas porosity; (5) repeat steps (3) and (4) for the whole tidal cycle; (6) calculate the resultant acoustic velocity and attenuation coefficient by summing all components of X_* and Y_* for each water depth (see equations (A6) and (A7)).

[45] The results are shown as the thick dashed lines in Figure 9b (attenuation coefficient) and in Figure 9c and Figure 9d (velocity). Figure 6c and Figure 6d show the model predictions of compressional wave velocity and attenuation coefficient for the whole 24 hour observation period (H2-H3 only).

6.5. Model Results

[46] The results of the single bubble size fitting exercise for shot 1 in Table 3 indicate gas bubble radii between 5.3 mm and 19.5 mm and associated porosities between 0.26% and 1.63% for each bubble size. These are reasonable numbers on the basis of observations of the X-ray CT scans in section 5.3. The cumulative gas porosity in Figure 10 suggests gas cavities occupy about 6% of the sediment volume.

[47] The model correctly predicts increasing resonance frequency of peaks A–E in Figure 9a and Figure 9b with increasing hydrostatic pressure (and vice versa; see Figure 6c). The magnitude of the attenuation coefficients are broadly in agreement with those measured in situ. A detailed comparison of observed (peaks A–E) and modeled frequency and attenuation shifts from low to high tide is given in Table 4. In all cases, except for peak A, the model underestimates the frequency shift. The model significantly underestimates the magnitude of the attenuation shift for peaks A, B, and E, while it is similar for peaks C and D (although opposite in polarity).

[48] The predicted acoustic phase velocity at low and high tide (Figure 9c and Figure 9d) are generally much higher than the observed velocities that remain well below the velocity of the water-saturated sediment over the whole frequency band. However, it is possible that the data ''dropouts'' at about 1000 Hz in Figure 9c and Figure 9d are due to poor signal-to-noise ratio because of extremely high attenuation. A poor signal-to-noise ratio may cause the cross-correlation step in the phase velocity calculation to correlate signal and noise.

Table 3. Model Predictions for Observed Resonance Peaks in Figure 9

		Observations		Model Predictions	
Experimental Details	Resonance Peak	Resonance Frequency, Hz	Attenuation Coefficient, dB m^{-1}	Bubble Radius, mm	Gas Porosity, %
Shot 1	A	700	180	19.49	1.63
Time = 0 hours	B	1050	214	13.04	1.10
Depth = 0 m	C	1650	188	8.33	0.39
	D	2100	175	6.56	0.23
	E	2600	227	5.31	0.26
Shot 32	A	750	128	18.20	0.72
Time = 5:10 hours	B	1250	182	10.97	0.58
Depth = 2.35 m	C	1950	194	7.06	0.31
	D	2350	180	5.87	0.20
	E	2800	187	4.93	0.16

Table 4. Comparison of Observed and Modeled Frequency Shifts Over Half a Tidal Cycle for Resonance Peaks in Figure 9

	Observations		Model Results	
Resonance Peak	Resonance Frequency Shift, Hz	Attenuation Shift, dB m^{-1}	Resonance Frequency Shift, Hz	Attenuation Shift, dB m^{-1}
A	50	−52	50	−4
B	200	−32	100	−6
C	300	6	100	−7
D	250	5	150	−8
E	200	−40	150	−10

These "1 kHz dropouts" support the idea of bubble resonance scattering at those frequencies. The fact that the observed velocities (500–700 m s^{-1}) remain well below the velocity of the water-saturated sediment at frequencies above the 1 kHz dropouts suggests that the observation frequency band is always below the resonance frequency of at least one bubble size population.

7. Discussion

[49] There is abundant evidence of shallow (~1 m) methane gas at the Dibden Bay site from chirp profiles and core samples. The sediments down to 3 m subseabed depth comprise anoxic gray mud with occasional sand-silt stringers, shelly layers, and abundant organic material. The data collected during an acoustic (vertical) transmission monitoring experiment there offer a fascinating insight into the acoustical behavior of shallow water, shallow subseabed, gassy marine sediments over the frequency range 600–3000 Hz.

[50] The attenuation maximum at 1050 Hz to 1250 Hz in Figure 6b is the most readily comparable observation to the *Anderson and Hampton* [1980a, 1980b] model. To our knowledge, this is the first time that a distinct gas bubble attenuation resonance peak has been observed in situ in marine sediments over a sufficiently wide bandwidth to describe the whole attenuation-frequency curve. Although other attenuation maxima are observed in Figure 9a and Figure 9b, this is the only one that shows a clearly discernible, continuous and systematic shift in resonance frequency between low tide and high tide in Figure 6. This exciting result raises the possibility of remotely sensing in situ gas bubble (and sediment) physical properties using acoustical methods. However, a suitably sophisticated model is required to interpret acoustic observations like these in terms of gas bubble size and shape, and their influence on the bulk acoustical and geotechnical properties of the sediment.

[51] The model predicts correctly that the attenuation maximum at 1050 Hz (low tide, shot 1 in Figure 9a) shifts to a higher frequency and a lower attenuation coefficient with increasing tidal height and to a lower frequency and a higher attenuation coefficient with decreasing tidal height. However, the model significantly underestimates the frequency shift (observed +200 Hz, model +100 Hz) and the attenuation shift (observed −32 dB m^{-1}, model −6 dB m^{-1}); see Table 4. The predictions for the other attenuation resonance peaks observed in the starting data set are less convincingly borne out by the observations in Figure 6b (H2 and H3), although Table 4 suggests a similar pattern of underestimated frequency and attenuation shift magnitudes. These could be due to a number of things not accounted for in the model, such as nonspherical bubbles, incorrect starting bubble size distribution and gas content, and gas diffusion. Another possibility is that of multiple resonance modes (frequencies) for gas bubbles in sediment, not considered here [see *Kargl et al.*, 1998]. It is also possible that some of these less convincing resonance peaks are in fact due to seabed/seafloor multiples (see sections 4.4 and 4.5).

[52] The X-ray CT results reveal the most obvious limitation of the model to be the assumption of spherical gas bubbles. While this is probably true for gas bubbles in sand-silt (see Figure 8a), this is certainly not the case for the majority of bubbles seen in the more argillaceous sediments (Figures 8b and 8c) that are crack-like. However, if we consider each modeled bubble radius to be the radius of a sphere of equivalent volume to the in situ gas bubble (whatever shape it may be), then the results should be broadly applicable. Nonspherical bubbles are more likely to affect acoustical anisotropy (not measured here).

[53] The gas bubble size distribution in Figure 10 contains bubble sizes smaller than 4 mm that have resonance frequencies above 3 kHz, although they account for only a very small fraction of the total gas volume according to Figure 10 (see also Table 3). Perhaps in reality bubble radii less than about 4 mm are more abundant than indicated here, or seen in the X-ray CT images in Figure 8 (issues of image resolution and reproducibility of in situ pressure and temperature conditions during X-ray CT scanning). If so, these smaller bubbles could have a more pronounced effect on velocity than that predicted here (there is some evidence that small bubbles affect the ultrasound velocities of the pressure core in Figure 7). This bubble size distribution was fitted only to the initial attenuation observations. Clearly, the model implementation could benefit from a quantitative study of the X-ray CT scans for a better estimate of in situ gas bubble size distribution.

[54] Another effect not considered is the possibility that a large gas bubble may split into two or three smaller bubbles as it shrinks, which then coalesce into a single bubble during expansion. This would give rise to relatively sudden changes in the bubble size distribution (although not in gas content) with time that could give rise to sudden changes in acoustical response. Also, the mean bubble size may continue to increase over several pressure cycles due to rectified diffusion, but investigations indicate that tidal variations are of too low a frequency for this to be a significant mechanism [*Boudreau et al.*, 2001].

[55] Recent studies of the acoustical behavior of gassy sediments [*Gardner*, 2000, 2003; *Gardner and Sills*, 2001] compared the *Anderson and Hampton* [1980a, 1980b] model to laboratory acoustic data in the frequency range 10 kHz to 1 MHz. Bubble size distributions were also incorporated in the model; all samples had bubble diameters less than 2 mm. These studies demonstrated the sensitivity of the Anderson and Hampton model to the elastic and damping properties of the sediment into which the model superimposes the acoustical effects of gas bubble resonance [see also *Wheeler and Gardner*, 1989]. However, it is interesting to note that for sediments with

gas contents above 8%, the Anderson and Hampton model significantly overestimated laboratory-measured velocities and gave good agreement with laboratory-measured attenuation coefficients (at least at and above resonance). These findings are consistent with our in situ observations and model comparisons.

8. Conclusions

[56] Attenuation results from an acoustic transmission monitoring experiment in shallow gassy marine sediments provide firm evidence for gas bubble resonance in situ. A strong resonance attenuation peak of 214 dB m^{-1} at a frequency of 1050 Hz at a water depth of 0 m shifts to 182 dB m^{-1} at 1250 Hz at 2.35 m. The *Anderson and Hampton* [1980a, 1980b] model predicts for this resonant peak an equivalent bubble radius and gas porosity of 13 mm and 1.1%, respectively, at a water depth of 0 m and 11 mm and 0.6%, respectively, at 2.35 m. X-ray CT scan images of a pressure-sealed core from the site show subspherical (sometimes coalescing) voids in silty sand up to ~10 mm in diameter and crack-like voids (longest axis in subvertical orientation) up to ~40 mm long (intermediate axis) in clayey silt. These suggest the acoustical model predictions are reasonable. The Anderson and Hampton model, taking into account a range of gas bubble sizes and changes in hydrostatic pressure, predicts the general trend of shifts in attenuation and frequency of this resonance attenuation peak over a complete tidal cycle but underestimates the magnitudes of the shifts. This could be due to phenomena not accounted for in the model, such as nonspherical bubbles, bubble coalescence, and gas diffusion. It could also be due to incorrect modeling of the water-saturated sediment elastic and damping properties on which the acoustical effect of bubbles is superimposed.

[57] Despite this, the results provide for the first time direct evidence for acoustical gas bubble resonance in situ in marine sediments over a sufficiently wide bandwidth to describe the frequency response curves of phase velocity and attenuation coefficient. These observations are consistent with our current theoretical understanding of gas bubble resonance in marine sediments.

Appendix A

[58] The following expressions were used to calculate acoustic velocity V and attenuation α in gassy marine sediments with a distribution of gas bubbles sizes [after *Anderson and Hampton*, 1980a, 1980b; *Andreeva*, 1964; *Devin*, 1959; *Eller*, 1970; *Meyer et al.*, 1958; *Minnaert*, 1933; *Silberman*, 1957; *Spitzer*, 1943; *Weston*, 1967].

$$\left(\frac{V_0}{V}\right)^2 = \frac{1 + a_s X_M}{2}\left\{1 \pm \left[1 + \left(\frac{a_s Y_M}{1 + a_s X_M}\right)^2\right]^{1/2}\right\}, \quad \text{(A1)}$$

and

$$\alpha = \frac{\pi f}{V_0}.\frac{V}{V_0}.\, a_s Y_M, \quad \text{(A2)}$$

where

$$a_s = \frac{K}{\gamma P_0 + 4/3 G}, \quad \text{(A3)}$$

$$X_* = \frac{n_g\left(1 - f_*^2\right)}{\left(1 - f_*^2\right)^2 + d_*^2}, \quad \text{(A4)}$$

$$Y_* = \frac{n_g d_*}{\left(1 - f_*^2\right)^2 + d_*^2}, \quad \text{(A5)}$$

$$X_M = \sum X_* = \sum_{i=1}^{m} \frac{n_{gi}\left(1 - f_{*i}^2\right)}{\left(1 - f_{*i}^2\right)^2 + d_{*i}^2}, \quad \text{(A6)}$$

$$Y_M = \sum Y_* = \sum_{i=1}^{m} \frac{n_{gi} d_{*i}}{\left(1 - f_{*i}^2\right)^2 + d_{*i}^2}, \quad \text{(A7)}$$

$$d_* = d f_*^2, \quad \text{(A8)}$$

$$d = d_t + d_r + d_f, \quad \text{(A9)}$$

$$d_t = B, \quad \text{(A10)}$$

$$d_r = kr. \quad \text{(A11)}$$

Note that equation (A11) differs from the expression published by *Anderson and Hampton* [1980a, equation (43)]. There is no special off-resonance behavior of the radiation damping term d_r, and hence the $(\omega_0/\omega)^2$ term should be omitted (personal communication, A. L. Anderson, 2001).

$$d_f = \frac{4G'}{\rho \omega_0^2 r^2}, \quad \text{(A12)}$$

$$f_* = \frac{f}{f_0}, \quad \text{(A13)}$$

$$f_0 = \frac{1}{2\pi r}\left(\frac{3\gamma P_0}{A\rho} + \frac{4G}{\rho}\right)^{1/2}, \quad \text{(A14)}$$

$$A = \left(1 + B^2\right)\left[1 + \frac{3(\gamma - 1)}{X}\left(\frac{\sinh X - \sin X}{\cosh X - \cos X}\right)\right], \quad \text{(A15)}$$

$$B = 3(\gamma - 1) \cdot \left(\frac{X(\sinh X + \sin X) - 2(\cosh X - \cos X)}{X^2(\cosh X - \cos X) + 3X(\gamma - 1)(\sinh X - \sin X)} \right), \quad \text{(A16)}$$

$$X = r\sqrt{\frac{2\omega\rho_g s_p}{C_g}}. \quad \text{(A17)}$$

Notation

- α acoustic attenuation coefficient in gassy sediment, dB m^{-1}.
- γ ratio of the specific heat capacity of methane gas at constant pressure to that at constant volume.
- λ acoustic wavelength, m.
- ρ density of sediment, kg m^{-3}.
- ρ_g density of gas, kg m^{-3}.
- ρ_w density of seawater, kg m^{-3}.
- ω_0 angular resonance frequency, rad s^{-1}.
- ω angular frequency, rad s^{-1}.
- δl difference in path length between multiple and direct arrivals, m.
- δt lag time (cross-correlation result) for two band-pass-filtered time series recorded at, e.g., H1 and H2, s.
- δx difference in source-receiver distances of hydrophone pairs (e.g., $x_2 - x_1$), m.
- a_s see equation (A3).
- A gas polytropic coefficient.
- A_1, A_2 rms energy of the band-pass-filtered time series recorded at, e.g., H1 and H2, V.
- B see equation (A16).
- c average acoustic wave phase velocity, m s^{-1}.
- c_0 concentration of gas in pore water at bubble radius r, mol m^{-3}.
- c_1 ambient gas concentration, mol m^{-3}.
- c_g concentration of gas in bubble, mol m^{-3}.
- C_g thermal conductivity of gas, J s^{-1} m^{-1} °C^{-1}.
- d bubble damping(=Q^{-1}).
- d_* see equation (A8).
- d_f bubble damping due to fluid viscosity.
- d_r bubble damping due to radiation.
- d_t bubble damping due to thermal properties of gas.
- D diffusivity corrected for tortuosity, m^2 s^{-1}.
- f frequency of acoustic signal, Hz.
- f_i interference fringe frequency, Hz.
- f_0 resonance frequency, Hz.
- f_* see equation (A13).
- G dynamic shear modulus of water-saturated sediment, Pa.
- G' imaginary part of complex shear modulus, Pa.
- i, m index terms in equations (A6) and (A7).
- k acoustic wave number in bubble-free sediment.
- K bulk modulus of water-saturated sediment, Pa.
- K_f bulk modulus of framework of mineral grains, Pa.
- K_s bulk modulus of mineral grains, Pa.
- K_w bulk modulus of pore water, Pa.
- L gas diffusion distance, m.
- n sediment porosity, fractional.
- n_g gas content, fractional.
- P_0 ambient hydrostatic pressure, Pa.
- P initial pressure, Pa.
- P_1 final pressure, Pa.
- Q quality factor.
- Q_g see equations (9) and (10).
- r bubble radius, m.
- r_0 initial gas bubble radius, m.
- r_1 final gas bubble radius, m.
- R distance between gas bubbles ($R \gg r$), m.
- S rate of methanogenesis, mol s^{-1}.
- s_p specific heat of gas at constant pressure, J kg^{-1} °C^{-1}.
- t time, s.
- T_1, T_2 start times of the windowed time series corresponding to, e.g., H1 and H2, s.
- V acoustic phase velocity in gassy sediment, m s^{-1}.
- V_0 acoustic phase velocity in nongassy sediment, m s^{-1}.
- V_p compressional wave velocity of sediment, m s^{-1}.
- V_s shear wave velocity of sediment, m s^{-1}.
- X see equation (A17).
- x_1, x_2 source-receiver distances for, e.g., H1, H2, m.
- X_*, Y_* frequency-dependent variables incorporating gas fraction and damping for a single gas bubble size.
- X_M, Y_M frequency-dependent variables incorporating gas fraction and damping for a distribution of gas bubble sizes.

[59] **Acknowledgments.** This work was funded by the Natural Environment Research Council (Michael Tuffin CASE Ph.D. studentship GT04/98/272/ES) and the Challenger Division for Seafloor Processes of the Southampton Oceanography Centre with EC support (COSTA EVK3-CT-1999-00006, EUROSTRATAFORM EVK3-CT-2002-00079). Thanks are extended to Associated British Ports (Southampton) for granting access to the field site and for the tide data, to Andy Harris, Simon Dean, Gary Robb, Stephanie Arnott, and Sally Marine for fieldwork assistance, and to Peter Schultheiss, Quentin Huggett, and John Roberts of Geotek Limited for pressure corer expertise.

References

Abegg, F., and A. L. Anderson (1997), The acoustic turbid layer in muddy sediments of Eckernförde Bay, Western baltic: Methane concentration, saturation and bubble characteristics, *Mar. Geol.*, *137*(1/2), 137–147.

Anderson, A. L., and L. D. Hampton (1980a), Acoustics of gas-bearing sediments I. Background, *J. Acoust. Soc. Am.*, *67*(6), 1865–1889.

Anderson, A. L., and L. D. Hampton (1980b), Acoustics of gas-bearing sediments. II. Measurements and models, *J. Acoust. Soc. Am.*, *67*(6), 1890–1903.

Anderson, A. L., F. Abegg, J. A. Hawkins, M. E. Duncan, and A. P. Lyons (1998), Bubble populations and acoustic interaction with the gassy floor of Eckernförde Bay, *Cont. Shelf Res.*, *18*, 1807–1838.

Andreeva, I. B. (1964), Scattering of sound by air bladders of fish in deep sound-scattering ocean layers, *Sov. Phys. Acoust.*, *10*, 17–20.

Best, A. I., and D. G. Gunn (1999), Calibration of multi-sensor core logger measurements for marine sediment acoustic impedance studies, *Mar. Geol.*, *160*(1–2), 137–146.

Best, A. I., Q. J. Huggett, and A. J. K. Harris (2001), Comparison of in-situ and laboratory acoustic measurements on Lough Hyne marine sediments, *J. Acoust. Soc. Am.*, *110*(2), 695–709.

Boudreau, B. P., B. S. Gardiner, and B. D. Johnson (2001), Rate of growth of isolated bubbles in sediments with a diagenetic source of methane, *Limnol. Oceanogr.*, *46*(3), 616–622.

Boyce, R. E. (1976), Definitions and laboratory techniques of compressional sound velocity parameters and wet water content, bulk density, and porosity parameters by gravimetric and gamma-ray attenuation techniques, *Initial Rep. Deep Sea Drill. Proj.*, *33*, 931–958.

Briggs, K. B., and M. D. Richardson (1996), Variability in in situ shear strength of gassy muds, *Geo Mar. Lett.*, *16*(3), 189–195.

British Standards Institution (1990), *British Standard Methods of Test for Soils for Civil Engineering Purposes*, *BS1377*, London.

Buckingham, M. J. (1998), Theory of acoustic attenuation, dispersion, and pulse propagation in unconsolidated granular materials including marine sediments, *J. Acoust. Soc. Am.*, *102*(5), 2579–2596.

Cochonat, P., J.-P. Cadet, S. J. Lallemant, S. Mazzotti, H. Nouzé, C. Fouchet, and J.-P. Foucher (2002), Slope instabilities and gravity processes in fluid migration and tectonically active environment in the eastern Nankai accretionary wedge (KAIKO-Tokai '96 cruise), *Mar. Geol.*, *187*, 193–202.

Courtney, R. C., and L. A. Mayer (1993), Calculation of acoustic parameters by a filter-correlation method, *J. Acoust. Soc. Am.*, *93*(2), 1145–1154.

Craig, R. F. (1992), *Soil Mechanics*, 427 pp., Chapman and Hall, New York.

Devin, C. (1959), Survey of thermal, radiation, and viscous damping of pulsating air bubbles in water, *J. Acoust. Soc. Am.*, *21*(12), 1654–1667.

Eller, A. I. (1970), Damping constants of pulsating bubbles, *J. Acoust. Soc. Am.*, *47*(5), 1469–1471.

Engleman, E. E., L. L. Jackson, and D. R. Norton (1985), Determination of carbonate carbon in geological materials by coulometric titration, *Chem. Geol.*, *53*, 125–128.

Fleischer, P., T. H. Orsi, M. D. Richardson, and A. L. Anderson (2001), Distribution of free gas in marine sediments: A global overview, *Geo Mar. Lett.*, *21*, 103–122.

Floodgate, G. D., and A. G. Judd (1992), The origins of shallow gas, *Cont. Shelf Res.*, *12*(10), 1145–1156.

Fu, S. S., R. H. Wilkens, and L. N. Frazer (1996), In situ velocity profiles in gassy sediments: Kiel Bay, *Geo Mar. Lett.*, *16*, 249–253.

Gardner, T. N. (2000), An acoustic study of soils that model seabed sediments containing gas bubbles, *J. Acoust. Soc. Am.*, *107*(1), 163–176.

Gardner, T. (2003), Modeling signal loss in surficial marine sediments containing occluded gas, *J. Acoust. Soc. Am.*, *113*(3), 1368–1378.

Gardner, T. N., and M. J. Goringe (1988), The measurement of gas bubble size distributions in a three-phase laboratory gassy soil, *Geotech. Test. J.*, *11*(1), 49–55.

Gardner, T. N., and G. C. Sills (2001), An examination of the parameters that govern the acoustic behavior of sea bed sediments containing gas bubbles, *J. Acoust. Soc. Am.*, *110*(4), 1878–1889.

Gassmann, F. (1951), Elastic waves through a packing of spheres, *Geophysics*, *16*, 673–685.

Gunn, D. E., and A. I. Best (1998), A new automated nondestructive system for high resolution multi-sensor core logging of open sediment cores, *Geo Mar. Lett.*, *18*, 70–77.

Hamilton, E. L. (1971), Elastic properties of marine sediments, *J. Geophys. Res.*, *76*(2), 579–604.

Hamilton, E. L. (1980), Geoacoustic modelling of the seafloor, *J. Acoust. Soc. Am.*, *68*(5), 1313–1340.

Hamilton, E. L., and R. T. Bachman (1982), Sound velocity and related properties of marine sediments, *J. Acoust. Soc. Am.*, *72*(6), 1891–1904.

Kargl, S. G., K. L. Williams, and R. Lim (1998), Double monopole resonance of a gas-filled, spherical cavity in a sediment, *J. Acoust. Soc. Am.*, *103*(1), 265–274.

Kaye, G. W. C., and T. H. Laby (1995), *Tables of Physical and Chemical Constants*, 611 pp., Addison-Wesley-Longman, Reading, Mass.

Kibblewhite, A. C. (1989), Attenuation of sound in marine sediments: A review with emphasis on new low-frequency data, *J. Acoust. Soc. Am.*, *86*(2), 716–738.

Lyons, A. P., M. E. Duncan, and A. L. Anderson (1996), Predictions of the acoustic scattering response of free-methane bubbles in muddy sediments, *J. Acoust. Soc. Am.*, *99*(1), 163–172.

Manley, P. L., and R. D. Flood (1989), Anomalous sound velocities in near-surface, organic-rich, gassy sediments in the central Argentine Basin, *Deep Sea Res., Part A*, *36*(4), 611–623.

McManus, J. (1991), Grain size determination and interpretation, in *Techniques in Sedimentology*, edited by M. Tucker, pp. 63–85, Blackwell Sci., Malden, Mass.

Meyer, E., K. Brendel, and K. Tamm (1958), Pulsation oscillations of cavities in rubber, *J. Acoust. Soc. Am.*, *30*(12), 1116–1124.

Mienert, J., and J. Posewang (1999), Evidence of shallow- and deep-water gas hydrate destabilizations in North Atlantic polar continental margin sediments, *Geo Mar. Lett.*, *19*(1/2), 143–149.

Minnaert, M. (1933), On musical air bubbles and the sounds of running water, *Philos. Mag.*, *16*, 235–248.

Orsi, T. H., C. M. Edwards, and A. L. Anderson (1994), X-ray computed tomography: A non-destructive method for quantitative analysis of sediment cores, *J. Sediment. Res., Sect. A*, *64*, 690–693.

Pujol, J. M., E. Luschen, and Y. Hu (1998), Seismic wave attenuation in metamorphic rocks from VSP data recorded in Germany's continental super-deep borehole, *Geophysics*, *63*(2), 354–365.

Schubel, J. R. (1974), Gas bubbles and the acoustically impenetrable, or turbid, character of some estuarine sediments, in *Natural Gases in Marine Sediments*, edited by I. R. Kaplan, pp. 275–298, Plenum, New York.

Schultheiss, P. J., and P. P. E. Weaver (1992), Multi-sensor core logging for science and industry, in *Oceans 92*, pp. 608–613, Inst. of Electr. and Electron. Eng., New York.

Shepard, F. P. (1954), Nomenclature based on silt-sand-clay ratios, *J. Sediment. Petrol.*, *24*, 151–158.

Shirley, D. J., and L. D. Hampton (1978), Shear-wave measurements in laboratory sediments, *J. Acoust. Soc. Am.*, *63*(2), 607–613.

Silberman, E. (1957), Sound velocity and attenuation in bubbly mixtures measured in standing wave tubes, *J. Acoust. Soc. Am.*, *29*(6), 925–933.

Sills, G. C., and S. J. Wheeler (1992), The significance of gas for offshore operations, *Cont. Shelf Res.*, *12*(10), 1239–1250.

Slowey, N. C., W. R. Bryant, and D. N. Lambert (1996), Comparison of high-resolution seismic profiles and the geoacoustic properties of Eckernförde Bay sediments, *Geo Mar. Lett.*, *16*, 240–248.

Spitzer, L. J. (1943), Acoustic properties of gas bubbles in a liquid, Div. of War Res., Columbia Univ., New York.

Stein, R. (1985), Rapid grain-size analysis of clay and silt fraction by Sedigraph 5000D: Comparison with Coulter counter and Atterberg methods, *J. Sediment. Petrol.*, *55*(4), 590–593.

Stoll, R. D. (1985), Marine sediment acoustics, *J. Acoust. Soc. Am.*, *77*(5), 1789–1799.

Stoll, R. D. (2002), Velocity dispersion in water-saturated granular sediment, *J. Acoust. Soc. Am.*, *11*(2), 785–793.

Tang, D. (1996), Modeling high-frequency acoustic backscattering from gas voids buried in sediments, *Geo Mar. Lett.*, *16*(3), 261–265.

Toksöz, M. N., and D. H. Johnston (Ed.) (1981), *Seismic Wave Attenuation*, *Geophys. Reprint Ser.*, vol. 2, pp. 1–5, Soc. of Explor. Geophys., Tulsa, Okla.

Tuffin, M. D. J. (2001), The geoacoustic properties of shallow, gas-bearing sediments, Ph.D. thesis, Univ. of Southampton, Southampton, UK.

Tuffin, M. D. J., A. I. Best, J. K. Dix, and J. M. Bull (2000), Acoustic characterization of gassy marine sediments in Dibden Bay, Southampton Water (UK), in *Fifth European Conference on Underwater Acoustics*, edited by M. E. Zakharia, P. Chevret, and P. Dubail, pp. 825–830, Eur. Comm., Lyon, France.

Wang, K., E. E. Davis, and G. van der Kamp (1998), Theory for the effects of free gas in subsea formations on tidal pore pressure variations and seafloor displacements, *J. Geophys. Res.*, *103*(B6), 12,339–12,353.

Weaver, P. P. E., and P. J. Schultheiss (1990), Current methods for obtaining, logging and splitting marine sediment cores, *Mar. Geophys. Res.*, *12*, 85–100.

Weston, D. E. (1967), Sound propagation in the presence of bladder fish, in *Underwater Acoustics*, edited by V. M. Albers, pp. 55–88, Plenum, New York.

Wever, T. F., F. Abegg, H. M. Fiedler, G. Fechner, and I. H. Stender (1998), Shallow gas in the muddy sediments of Eckernförde Bay, *Germany, Cont. Shelf Res.*, *18*(14–15), 1715–1739.

Wheeler, S. J. (1988), A conceptual model for soils containing large gas bubbles, *Géotechnique*, *38*(3), 389–397.

Wheeler, S. J., and T. N. Gardner (1989), Elastic moduli of soils containing gas bubbles, *Géotechnique*, *39*(2), 333–342.

Wheeler, S. J., W. K. Sham, and S. D. Thomas (1990), Gas pressure in unsaturated offshore soils, *Can. Geotech. J.*, *27*, 79–89.

Whelan, T., J. M. Coleman, H. H. Roberts, and J. N. Suhayda (1976), The occurrence of methane in recent deltaic sediments and its effect on soil stability, *Bull. Int. Assoc. Eng. Geol.*, *14*, 55–64.

Wilkens, R. H., and M. D. Richardson (1998), The influence of gas bubbles on sediment acoustic properties: In situ, laboratory, and theoretical results from Eckernförde Bay, Baltic Sea, *Cont. Shelf Res.*, *18*, 859–892.

A. I. Best and M. D. J. Tuffin, Challenger Division for Seafloor Processes, Southampton Oceanography Centre, University of Southampton Waterfront Campus, European Way, Southampton SO14 3ZH, UK. (aib@soc.soton.ac.uk)

J. M. Bull and J. K. Dix, School of Ocean and Earth Science, Southampton Oceanography Centre, University of Southampton Waterfront Campus, European Way, Southampton SO14 3ZH, UK.